FULL PAPER

Batteries

ADVANCED
ENERGY
MATERIALS

www.advenergymat.de

Native Vacancy Enhanced Oxygen Redox Reversibility and Structural Robustness

Yejing Li, Xuefeng Wang, Yurui Gao, Qinghua Zhang, Guoqiang Tan, Qingyu Kong, Seongmin Bak, Gang Lu, Xiao-Qing Yang, Lin Gu, Jun Lu, Khalil Amine, Zhaoxiang Wang,* and Liquan Chen

Cathode materials with high energy density, long cycle life, and low cost are of top priority for energy storage systems. The Li-rich transition metal (TM) oxides achieve high specific capacities by redox reactions of both the TM and oxygen ions. However, the poor reversible redox reaction of the anions results in severe fading of the cycling performance. Herein, the vacancy-containing $Na_{4/7}[Mn_{6/7}(\square_{Mn})_{1/7}]O_2$ ($\square_{Mn}$ for vacancies in the Mn—O slab) is presented as a novel cathode material for Na-ion batteries. The presence of native vacancies endows this material with attractive properties including high structural flexibility and stability upon Na-ion extraction and insertion and high reversibility of oxygen redox reaction. Synchrotron X-ray absorption near edge structure and X-ray photoelectron spectroscopy studies demonstrate that the charge compensation is dominated by the oxygen redox reaction and Mn^{3+}/Mn^{4+} redox reaction separately. In situ synchrotron X-ray diffraction exhibits its zero-strain feature during the cycling. Density functional theory calculations further deepen the understanding of the charge compensation by oxygen and manganese redox reactions and the immobility of the Mn ions in the material. These findings provide new ideas on searching for and designing materials with high capacity and high structural stability for novel energy storage systems.

1. Introduction

Energy storage systems (ESS) that are cost-effective and capable of running stably for years or decades are key to the large-scale application of the intermittent renewable energy resources. For most of the transition metal (TM) oxide cathode materials, charge compensation is realized by the reduction and oxidation of the TM ions during the electrochemical cycling. However, oxygen evolution prior to the full oxidation of the TM ions is often unavoidable due to the strong O-p/TM-d covalent hybridization.[1] Recent studies show that enhancing the strength of the TM—O bonds can stabilize the oxygen, which in turn helps to break through the bottleneck and achieve a higher capacity, as is expected for the Li-rich layered oxides.[2] However, the long-term reversibility of the oxygen redox reactions remains challenging though such reactions are really attractive. Oxygen oxidation was reported

Dr. Y. Li, Dr. X. Wang, Prof. Z. Wang, Prof. L. Chen
Key Laboratory for Renewable Energy
Chinese Academy of Sciences
Institute of Physics
Chinese Academy of Sciences
P. O. Box 603, Beijing 100190, China
E-mail: zxwang@iphy.ac.cn, zxwang@aphy.iphy.ac.cn
Dr. Y. Li, Prof. Z. Wang, Prof. L. Chen
School of Physical Sciences
University of Chinese Academy of Sciences
P. O. Box 603, Beijing 100190, China
Dr. X. Wang
Department of NanoEngineering
University of California San Diego
9500 Gilman Drive, La Jolla, CA 92093, USA
Dr. Y. Gao, Prof. G. Lu
Department of Physics and Astronomy
California State University Northridge
Northridge, CA 91330-8268, USA

Dr. Q. Zhang, Prof. L. Gu
Laboratory for Advanced Materials & Electron Microscopy
Institute of Physics
Chinese Academy of Sciences
P. O. Box 603, Beijing 100190, China
Dr. G. Tan, Prof. J. Lu, Prof. K. Amine
Chemical Sciences and Engineering Division
Argonne National Laboratory
9700 S. Cass Avenue, Lemont, IL 60439, USA
Dr. Q. Kong
Synchrotron Soleil
L'Orme des Merisiers St-Aubin
91192, Gif-sur-Yvette Cedex, France
Dr. S. Bak, Prof. X.-Q. Yang
Chemistry Department
Brookhaven National Laboratory
Upton, NY 11973, USA

ADVANCED
SCIENCE NEWS
www.advancedsciencenews.com

ADVANCED
ENERGY
MATERIALS
www.advenergymat.de

in layered oxides, but is usually accompanied with generation of oxygen vacancies and resultant migration of the TM ions.[3] Such structural instability results in poor electrochemical performances including fast capacity decay and severe voltage fading.[4] Tarascon and co-workers[5] proposed Li_3IrO_4 as a new cathode material that can reversibly uptake or release 3.5 electrons per Ir^{5+} ion, close to the limit of the oxygen redox. Nevertheless, this material is unstable against O_2 release upon removal of the Li ions. Lu and co-workers[6] recently reported antifluorite Li_4FeO_5 as a novel cathode material, in which reversible redox reactions occur on both the anion and the cation with no obvious oxygen release between 1.0 and 4.7 V. However, significant structural transformation takes place during its initial charging. More recently, we stabilized the structure of Li- and Mn-rich layer-structured $Li_{1.2}Mn_{0.54}Ni_{0.13}Co_{0.13}O_2$ ($0.5Li_2MnO_3 \cdot 0.5LiNi_{1/3}Co_{1/3}Mn_{1/3}O_2$) by deactivating the surface oxygen by surface doping (≈5 atomic layers) of Nb^{5+}, Ti^{4+}, and Zr^{4+} ions.[7] Except for the hybrid charge compensation by the TM and O, Li and co-workers[8] presented an exclusive anion redox reaction of nanolithia ($Li_2O \leftrightarrow Li_2O_2 \leftrightarrow LiO_2$) in porous Co_3O_4. With the catalysis of the porous Co_3O_4, a discharge capacity of 587 mAh g^{-1} was obtained with stable cycling performance, illustrating the feasibility of oxygen redox for obtaining high-capacity cathode materials.

A robust structure with the fewest phase transitions is crucial to maintaining the cycling reversibility, especially when the oxygen redox reactions are involved. The other prerequisite to have a long cycle life is to confine the volume change of the electrode material, especially in the "rigid" solid-state batteries. In this sense, zero-strain materials are ideal for a battery electrode. The spinel $Li_4Ti_5O_{12}$ that experiences a series of phase transitions between $Li_4Ti_5O_{12}$ and $Li_7Ti_5O_{12}$[9] but with a volume change of less than 0.2–0.3% is a good example of such, ensuring its excellent stability for as long as thousands of cycles.[10] To date, a number of zero-stain electrode materials have been reported, including $P2-Na_{0.66}[Li_{0.22}Ti_{0.78}]O_2$ and $Na_3V(PO_3)_3N$ upon Na extraction or insertion.[11] However, the specific capacity of these materials is low. Hunting for zero-strain materials with high specific capacities is critical, especially for the cathode materials in which sodium (Na) or other large ions are extracted or inserted.

Na-ion batteries (NIBs) are regarded as a promising alternative to the Li-ion batteries (LIBs) in energy storage. In addition to the abundance of element Na, the TM with rich reserves can further decrease the cost of the ESS. Manganese (Mn)-based oxides are the ones and have been paid much attention in the past decades.[12] To date, $O3-NaMnO_2$, $P2-Na_{0.7}MnO_2$, and tunnel-type $Na_{0.44}MnO_2$ have been extensively studied. It was reported that $O3-NaMnO_2$ delivers a specific capacity of 200 mAh g^{-1} but undergoes complicated phase transitions and fast capacity fading in the subsequent cycles.[13] There is severe Jahn–Teller distortion in the structure of $P2-Na_{0.7}MnO_2$ due to the presence of the Mn^{3+} ions.[14] As for the tunnel-type $Na_{0.44}MnO_2$, the Mn^{3+} ions on the square-pyramidal sites cannot be oxidized to Mn^{4+}, resulting in a low specific capacity.[15] Thus, none of the above mentioned materials can meet the requirements of the ESSs to their cathode materials.

This article presents layer-structured vacancy-containing $Na_{4/7}[Mn_{6/7}(\square_{Mn})_{1/7}]O_2$ ($\square_{Mn}$ for vacancies in the Mn layer) as a state-of-the-art cathode material for high performance NIBs.

When it is cycled between 1.5 and 4.4 V versus Na^+/Na, a reversible capacity up to 220 mAh g^{-1} is obtained. With the native vacancies in the $[Mn_{6/7}(\square_{Mn})_{1/7}]O_2$ slabs, it shows negligible structural changes upon wide voltage-span cycling and during rigid oxygen redox reaction. Synchrotron X-ray absorption near edge structure (XANES) and X-ray photoelectron spectroscopy (XPS) studies demonstrate the charge compensation by the oxygen redox between 2.3 and 4.4 V and by the Mn^{3+}/Mn^{4+} redox between 1.5 and 2.3 V. The Raman spectroscopy, aberration-corrected scanning transmission electron microscopy (STEM), and extended X-ray absorption fine structure (EXAFS) demonstrate the high structural flexibility and stability of the $[Mn_{6/7}(\square_{Mn})_{1/7}]O_2$ slabs when 0.76 Na^+ ion per formula unit (Na f.u.$^{-1}$) is repeatedly extracted or inserted. Density functional theory (DFT) calculations explain the immobility of the oxygen and manganese ions during charge compensation. These findings provide new ideas on hunting and designing novel cathode materials with high capacity and structural stability for the NIBs and other high-energy-density secondary batteries.

2. Results and Discussion

The $Na_{4/7}[Mn_{6/7}(\square_{Mn})_{1/7}]O_2$ was synthesized by the solid-state reaction. X-ray diffraction (XRD) reveals that the as-prepared material is a phase-pure $Na_{4/7}[Mn_{6/7}(\square_{Mn})_{1/7}]O_2$ (PDF index 78-0193; **Figure 1**a). Its edge-sharing MnO_6 octahedrons build up the $[Mn_{6/7}(\square_{Mn})_{1/7}]O_2$ slabs, between which are located the Na ions in the form of NaO_6 polyhedrons (Figure 1b). More importantly, periodic $\square_{Mn}$ vacancies are contained in the $[Mn_{6/7}(\square_{Mn})_{1/7}]O_2$ slabs (Figure 1c). These features ensure its structural flexibility, which, in turn, enhances the structural stability when a large number of Na ions are inserted or extracted. In addition, this material is found very stable in air for as long as 12 months (Figure S1, Supporting Information), though its particles are rather small (≈50 nm in size) and well dispersed from the scanning electron microscopy (SEM) (Figure S2, Supporting Information).

When a $Na_{4/7}[Mn_{6/7}(\square_{Mn})_{1/7}]O_2$/Na cell was charged to 4.4 V from the open-circuit voltage (OCV) (≈2.75 V), $Na_{4/7}[Mn_{6/7}(\square_{Mn})_{1/7}]O_2$ delivers a capacity of 96 mAh g^{-1}, corresponding to the extraction of about 0.33 Na f.u.$^{-1}$. The corresponding voltage profile starts with a gentle slope and is followed with a plateau at 4.2 V (Figure 1d). Since the valence of the Mn ions in $Na_{4/7}[Mn_{6/7}(\square_{Mn})_{1/7}]O_2$ is +4, the charge compensation accompanying the Na-ion extraction at high voltage is supposed to be realized by the O^{2-} oxidation, similar to that in the Li-rich oxide cathode materials for the LIBs.[16] However, different from that of the Li-rich oxides, the plateau at the high voltage remains there in the subsequent charge processes. Actually, the voltage profile of the initial charge can completely overlap with that of the 2nd charge (by simple translation in Figure 1d). These imply that the oxidation of the material and its structural variation are reversible.

Cyclic voltammetry (CV) was recorded to identify the possible redox reactions (Figure S3, Supporting Information). Consistent with the voltage profiles, two strong anodic peaks appear around 2.2 and 4.2 V, corresponding to the oxidations of Mn^{3+} to Mn^{4+} and O^{2-} to $O^{(2-x)-}$, respectively, as will be clarified in the following discussion.
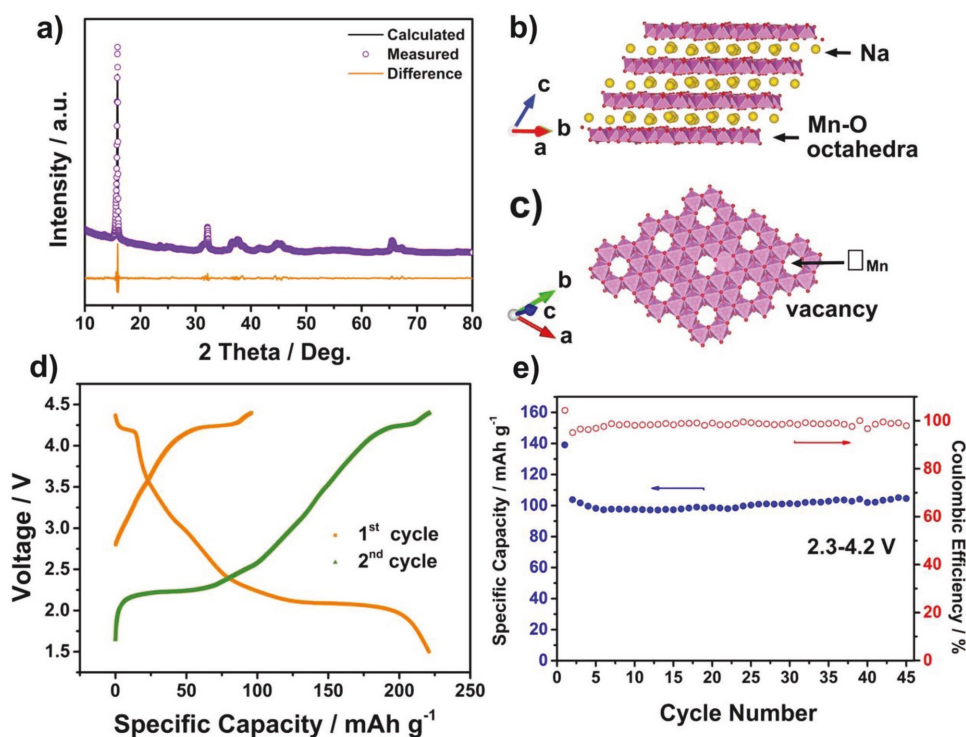
**ADVANCED
SCIENCE NEWS**

www.advancedsciencenews.com

**ADVANCED
ENERGY
MATERIALS**

www.advenergymat.de

Figure 1. a) XRD pattern of the as-prepared $Na_{4/7}[Mn_{6/7}(\square_{Mn})_{1/7}]O_2$. Schematic structure b) perpendicular to and c) along the (−110) direction. d) The voltage profile of $Na_{4/7}[Mn_{6/7}(\square_{Mn})_{1/7}]O_2$ initially charged to 4.4 V and then cycled between 1.5 and 4.4 V. e) The cycling performance of $Na_{4/7}[Mn_{6/7}(\square_{Mn})_{1/7}]O_2$ between 2.3 and 4.2 V.

2.1. Structural Evolution and Charge Compensation

In situ synchrotron XRD (λ = 0.1174 Å) was applied to recognize the structural evolution of $Na_{4/7}[Mn_{6/7}(\square_{Mn})_{1/7}]O_2$ upon Na-ion extraction and insertion. When the cell is charged to 4.4 V and then discharged to 1.5 V, the XRD patterns at different voltages seem the same and no new peak appears (**Figure 2**). The (−110) peak shifts ≈0.03° (2θ) toward the higher angle at the end of the initial charge, corresponding to a contraction of 0.01 Å of the interlayer distance between the two $[Mn_{6/7}(\square_{Mn})_{1/7}]O_2$ slabs. This is similar to the abrupt structural variation of the typical layered oxide $LiNi_{0.8}Co_{0.15}Al_{0.05}O_2$ when its lattice oxygen is oxidized at ≈4.0 V versus Li^+/Li.[17] In the subsequent discharge process, this diffraction first shifts to the lower angle and then goes back to the higher angle (total angle shifting ≈0.06°). This shifting is so trivial that it cannot be detected by the conventional XRD using the Cu Kα line (λ = 1.54 Å) (Figure S4, Supporting Information). The slight difference between these two X-rays is attributed to the higher quality (lower dispersion and higher collimation) and higher reciprocal space resolution of the synchrotron X-ray. Therefore, the structural variation of $Na_{4/7}[Mn_{6/7}(\square_{Mn})_{1/7}]O_2$ is negligible in the whole process, beneficial for enhancing its structural stability upon repeated cycling.

Advanced aberration-corrected STEM was employed to reveal the structural evolution upon Na extraction and insertion at the atomic scale both in high-angle annular dark-field (HAADF) and annular bright-field (ABF) methods. The typical layered structure and the native vacancy in the Mn−O slabs

(**Figure 3**a,b) of the as-prepared $Na_{4/7}[Mn_{6/7}(\square_{Mn})_{1/7}]O_2$ are clearly observed, with the Na ions in the interlayer between the $[Mn_{6/7}(\square_{Mn})_{1/7}]O_2$ slabs (Figure 3c,d). The interlayer distance is measured to be 5.5 Å according to the line scan intensity profile in the direction perpendicular to the layer (Figure S5, Supporting Information). None of the following processes can change the structural skeleton or the interlayer distance of this material, extraction of 0.33 Na f.u.$^{-1}$ (charged to 4.4 V, approximately $Na_{0.24}[Mn_{6/7}(\square_{Mn})_{1/7}]O_2$; Figure 3e,f), reinsertion of 0.76 Na f.u.$^{-1}$ (discharged to 1.5 V after initially charged to 4.4 V, approximately $Na_{1.0}[Mn_{6/7}Na_{1/7}]O_2$), or initial insertion of 0.43 Na ion (directly discharged to 1.5 V, approximately $Na[Mn_{6/7}Na_{1/7}]O_2$; Figure S6, Supporting Information). These observations demonstrate the negligible structural changes of $Na_{4/7}[Mn_{6/7}(\square_{Mn})_{1/7}]O_2$ during cycling, consistent with the in situ XRD results. The contrast of the Na ions in the Na layer decreases slightly after charge (Figure 3e,f) and increases after discharge (Figure 3g,h), corresponding to the extraction/insertion of the Na ions from/into the interlayer, respectively. In addition, no Mn-ion migration or surface reconstruction is observed (Figure S7, Supporting Information), different from the case of the Li-rich oxide materials.[18] This is important in keeping the surface structure and avoiding any irreversible surface-to-bulk propagation of the structural degradation, which lead to irreversible delays of specific capacity and discharge voltage. A combination of the XRD and STEM results demonstrates the excellent structural stability of $Na_{4/7}[Mn_{6/7}(\square_{Mn})_{1/7}]O_2$ both in the bulk and on the surface upon Na extraction and insertion.

**ADVANCED
SCIENCE NEWS**

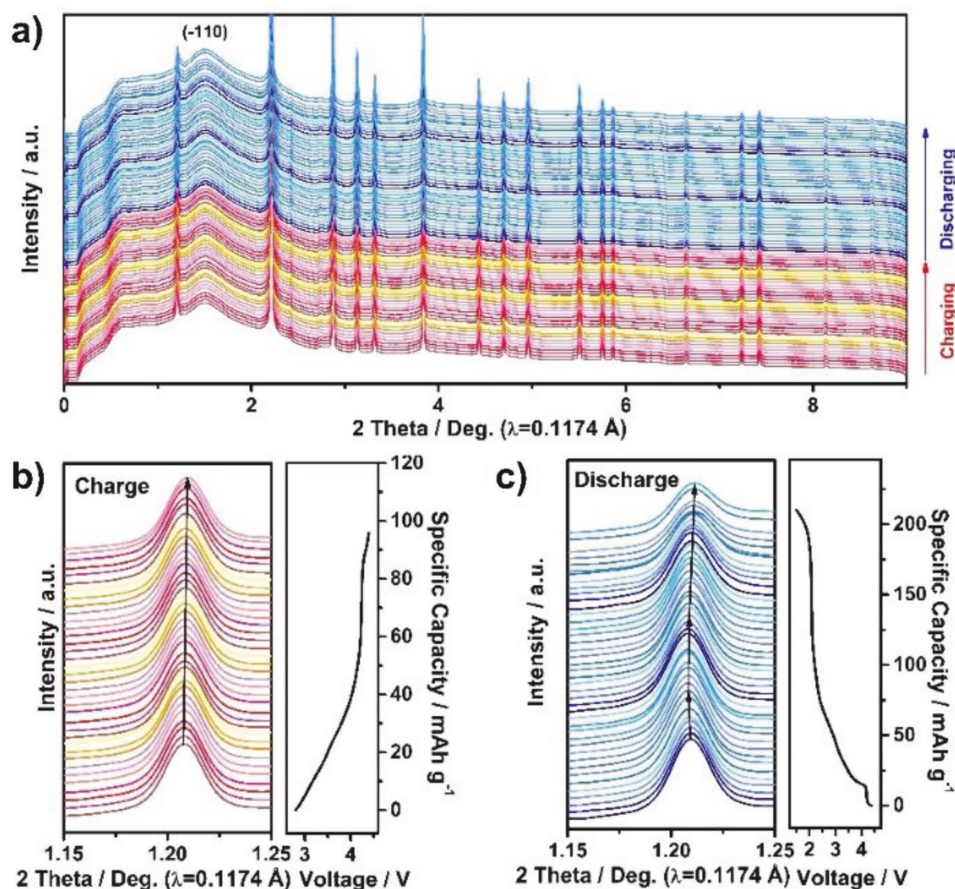www.advancedsciencenews.com

**ADVANCED
ENERGY
MATERIALS**

www.advenergymat.de

Figure 2. a) In situ synchrotron XRD (λ = 0.1174 Å) patterns for $Na_{4/7}[Mn_{6/7}(\square_{Mn})_{1/7}]O_2$ upon Na-ion extraction and insertion, the zoomed-in (−110) diffraction during b) charge and c) discharge.

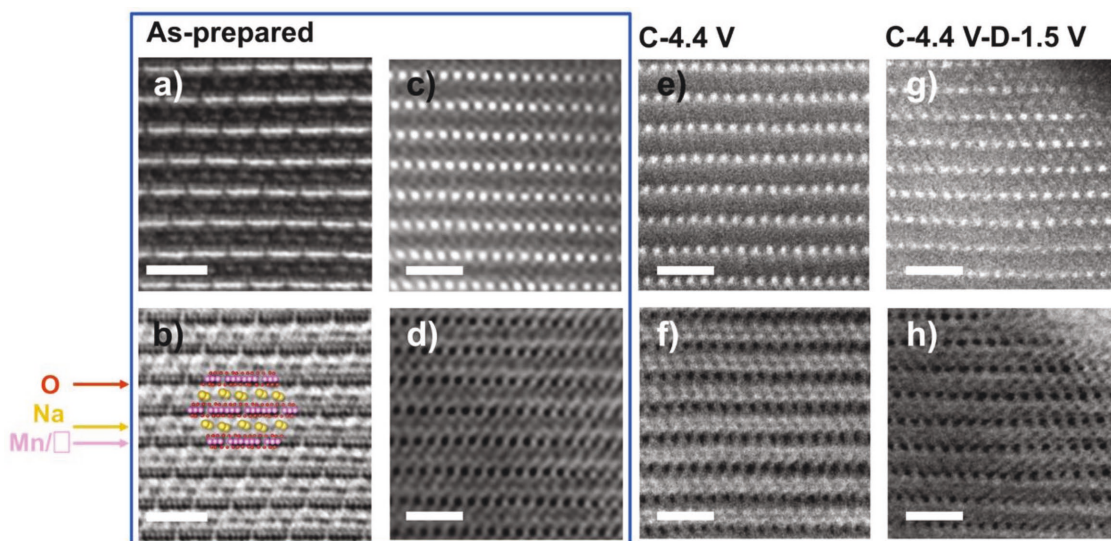**Figure 3.** The a,c,e,g) HAADF and b,d,f,h) ABF images of $Na_{4/7}[Mn_{6/7}(\square_{Mn})_{1/7}]O_2$ at various states: as-prepared (a–d), charged to 4.4 V (e and f), and charged to 4.4 V and then discharged to 1.5 V (g and h). The red, yellow, and pink balls in (b) represent the oxygen, sodium, and manganese atoms, respectively. The scale bar in each panel represents 1.0 nm. The zoom axis for (a and b) and (c–h) are [001] and [−110], respectively.
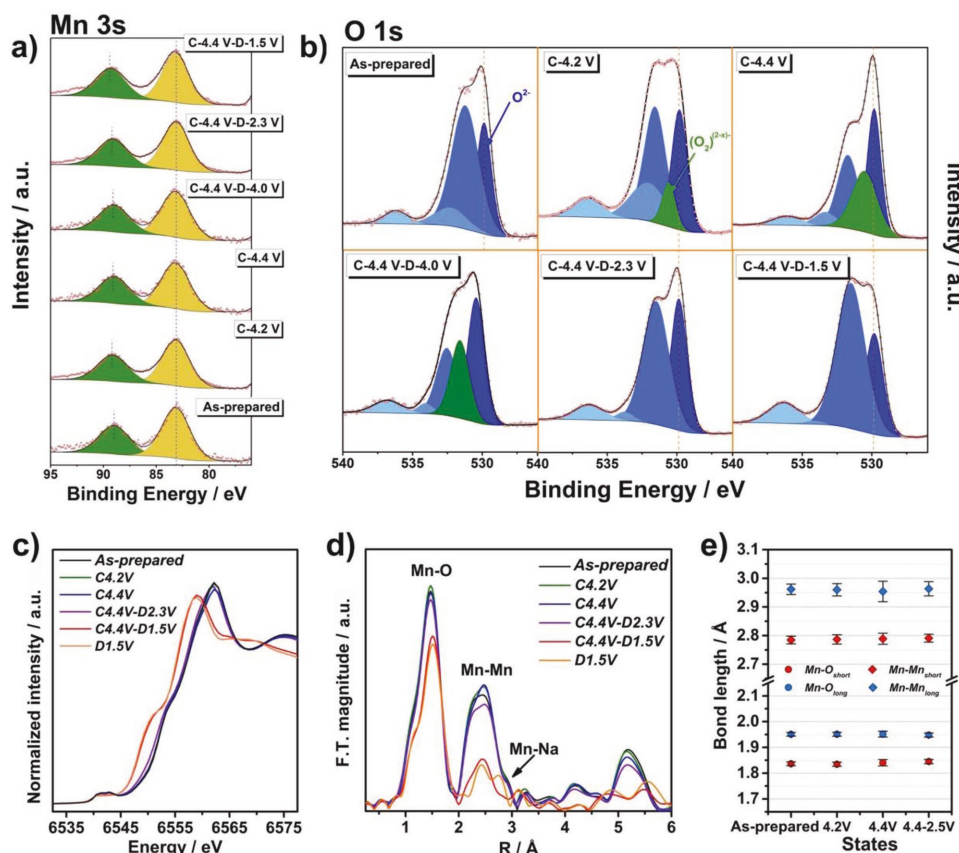
Figure 4. Evolution of the a,b) XPS, c) Mn K-edge XANES, and d) EXAFS spectra of $Na_{4/7}[Mn_{6/7}(\square_{Mn})_{1/7}]O_2$ at various charge/discharge states. e) The different bond lengths for the fitted EXAFS spectrum: red circles for $Mn-O_{short}$, blue circles for $Mn-O_{long}$, red squares for $Mn-Mn_{short}$, and blue squares for $Mn-Mn_{long}$.

The charge compensation mechanism was explored by XPS and synchrotron X-ray absorption spectroscopy (XAS). The spectra of Mn_{3s} (**Figure 4**a) and Mn_{2p} were combined to recognize the Mn oxidation since the signal-to-noise ratio of the Mn_{2p} spectrum (Figure S8, Supporting Information) is not high enough and the presence of its satellite peaks disturbs the analysis. The Mn_{3s} peak splits into two components due to the coupling of the nonionized 3s electrons with the 3d valence electrons. The splitting (energy difference of these two components, ΔE) was used to diagnose the oxidation state of the Mn ions. The splitting in the as-prepared $Na_{4/7}[Mn_{6/7}(\square_{Mn})_{1/7}]O_2$, $\Delta E = 4.8$ eV, well matches that of the Mn^{4+} ion.[19] No obvious changes of splitting are observed when $Na_{4/7}[Mn_{6/7}(\square_{Mn})_{1/7}]O_2$ is initially charged to 4.4 V and then discharged to 2.3 V. This means that the Mn^{4+} ions do not contribute to the charge compensation in this process. On the contrary, a new component emerges at 531.5 eV (the green peak) in the O_{1s} spectrum of the sample charged to 4.2 V. This component is assigned to the $O^{(2-x)-}$ species (Figure 4b). The content of the $O^{(2-x)-}$ species increases from 7.12% to 30.07% when $Na_{4/7}[Mn_{6/7}(\square_{Mn})_{1/7}]O_2$ is further charged from 4.2 to 4.4 V, suggesting that the plateau at around 4.2 V in Figure 1d corresponds to the O^{2-} oxidation. In the subsequent discharge process (discharged to 2.3 V), the newly emerged component disappears while the splitting of the Mn_{3s} spectrum increases to $\Delta E = 5.2$ eV, corresponding

to the formation of Mn^{3+}.[20] Therefore, the plateau at 2.2 V in Figure 1d is assigned to the Mn^{3+}/Mn^{4+} redox reaction.

The charge compensation and structural evolution of $Na_{4/7}[Mn_{6/7}(\square_{Mn})_{1/7}]O_2$ upon Na extraction and insertion are verified by XAS. As the cell is charged from 2.3 V (the OCV) to 4.4 V, the Mn K-edge in the XANES (Figure 4c) tilts slightly without any detectable shifting, illustrating that Na extraction does not change the chemical state of the Mn ion; it only induces some slight variation in the coordination environment of the Mn ions. These are consistent with the above XPS results, indicating the inertness of the Mn ions to the charge compensation above 2.3 V. As the Na ions are inserted (discharged to 1.5 V), the Mn K-edge shifts to the lower energy, indicating the reduction of the Mn ions.

The EXAFS was obtained by Fourier transformation (FT) of the XAS spectrum and employed to find out the coordination environment around the Mn ions and to clarify the structural evolution of $Na_{4/7}[Mn_{6/7}(\square_{Mn})_{1/7}]O_2$ during cycling (Figure 4d). No significant changes are found in the Mn−O bond length during cycling between 2.3 and 4.4 V. Some static ordering/disordering is observed in the 1st shell (Mn−O) and the 2nd shell (Mn−Mn). Due to the structural deformation of the fresh $Na_{4/7}[Mn_{6/7}(\square_{Mn})_{1/7}]O_2$ and the presence of the native vacancies in the $[Mn_{6/7}(\square_{Mn})_{1/7}]O_2$ slabs, the EXAFS peaks are asymmetric. This implies that all the Mn−O or Mn−Mn

bonds do not have the same length, different from that of, for example, the O3-type layered structures. Actually, there are six different Mn−O bond lengths and five different Mn−Mn bond lengths for the P1-type $Na_{4/7}[Mn_{6/7}(\square_{Mn})_{1/7}]O_2$. A simplified structure model with two different bond lengths (both Mn−O and Mn−Mn) was used to fit the EXAFS data (Figure S9, Supporting Information). The fitting quality is quite satisfactory (the R-factor is shown in Figure S10 in the Supporting Information). As expected, no obvious changes are observed in the bond length. The Mn−O bonding has higher degree of ordering than the Mn−Mn bonding, as smaller changes of the Debye–Waller factor than those for the Mn−Mn bond were obtained by the EXAFS fitting (Figure S10, Supporting Information). Slight changes of the FT magnitude is also shown in Figure 4d, corresponding to the variation of the coordination number. Tiny increase or decrease of the FT magnitude of the Mn−O, Mn−Mn, and Mn−Na shells indicates the slight changes of the coordination environment for Mn.

Insensitive to the crystallinity of a material, Raman scattering was undertaken to characterize the structural evolution of $Na_{4/7}[Mn_{6/7}(\square_{Mn})_{1/7}]O_2$ upon cycling (Figure S11, Supporting Information). The Raman peak at 638 cm^{-1} is attributed to the symmetric Mn−O stretching in the MnO$_6$ slab (the v_1 or A$_{1g}$ symmetric mode in the C_{2h}^3 space group). Its position remains there throughout the charge and discharge processes. The 580 cm^{-1} band is assigned to the Mn−O stretching in the basal plane of the [MnO$_6$] slab (v_2). It is usually related to the Mn^{4+} ions in the layered birnessite material.[21] Its position also keeps unchanged throughout this process until the sample is discharged to 1.5 V.

It deserves noticing that the Raman spectrum of the samples charged or discharged to 2.3 and 2.5 V, two states closest to the fresh $Na_{4/7}[Mn_{6/7}(\square_{Mn})_{1/7}]O_2$, is very similar to that of the as-prepared $Na_{4/7}[Mn_{6/7}(\square_{Mn})_{1/7}]O_2$ in position and in relative intensity. This means that the structure of the material restores after complicated and different charge/discharge processes. Therefore, the Raman spectroscopic study indicates that no significant structural changes occur and the structural changes are reversible, upon cycling of the material between 2.3 and 4.4 V, in good agreement with the XRD results.

2.2. DFT Calculations

DFT calculations were carried out to understand the structural stability and the charge compensation of $Na_{4/7}[Mn_{6/7}(\square_{Mn})_{1/7}]O_2$, especially for the reversible oxygen redox reactions, during the Na-ion extraction and insertion. On the basis of the calculated formation energy hull, we can derive the configurations of $Na_{4/7+x}Mn_{6/7}O_2$ ($-4/7 \leq x \leq 4/7$) at different sodiation/desodiation states (Figure S12, Supporting Information). It is found that the vacancy sites in the $[Mn_{6/7}(\square_{Mn})_{1/7}]O_2$ slab tend to be occupied by the Na ions once $x > 0$. This is beneficial for realizing a high capacity, thanks to the more available active sites. Impressively, the structure integrity remains even when all the active sites are occupied.

Analysis to the spin charge shows that the valence of the Mn ion is +4 in $Na_{4/7}[Mn_{6/7}(\square_{Mn})_{1/7}]O_2$ and remains +4 during charging ($x \leq 0$ in $Na_{4/7+x}[Mn_{6/7}(\square_{Mn})_{1/7}]O_2$; Figure S13a, Supporting Information). On the contrary, the Mn^{4+} ions

are reduced to Mn^{3+} as the Na ions are inserted ($x > 0$ in $Na_{4/7+x}[Mn_{6/7}(\square_{Mn})_{1/7}]O_2$; Figure S13b, Supporting Information). These results agree well with the above XPS and XANES analyses.

The O$_{2p}$ orbitals predominantly contribute to the density of states (DOS) near the Fermi level of $Na_{4/7}[Mn_{6/7}(\square_{Mn})_{1/7}]O_2$ and lose electrons as the Na ions are extracted ($x \leq 0$ in $Na_{4/7+x}[Mn_{6/7}(\square_{Mn})_{1/7}]O_2$; **Figure 5**a). This demonstrates that it is the oxygen that compensates for the charge change during Na extraction. Analysis of the charge distribution in two ranges, −0.45–0.0 and −0.75–0.0 eV of the Fermi level, further shows that it is the oxygen around the vacancies (configuration O−$\square_{Mn}$−O) that contributes to the charge compensation (Figure 5b,c). Ceder and co-workers[22] reported Li−O−Li configuration in the oxygen coordination with four Li ions and two Ni ions for LiNiO$_2$. In consistence with their report, we observed a significant O$_{2p}$ contribution to the charge compensation in O−$\square_{Mn}$ configuration. With this, we believe that the vacancies in the $[Mn_{6/7}(\square_{Mn})_{1/7}]O_2$ slabs introduce lone-pair electrons for the O$_{2p}$, raising its energy above the antibonding orbital t$_{2g}$, which is a hybridization of O$_{2p}$ and Mn$_{3d}$. Therefore, oxygen in the configuration of O−Mn−O will be oxidized during Na-ion extraction.

New hybridized states consisting of Mn$_{3d}$ and O$_{2p}$ orbitals appear near the Fermi level once the Na ions are inserted (from $x = 0$ to $x = 2/7$), due to the presence of the Mn^{3+} ion. With more Na ions inserted, the number of the hybridized state increases (Figure S14, Supporting Information). As more Na ions are inserted, the number of the hybrid states increases (Figure 3b), indicative of continuous reduction of the Mn^{4+} ions (Mn$^{4+} \rightarrow$ Mn^{3+}), echoed by the instead increase of Mn^{3+} ions from the spin charge analysis (Table S1, Supporting Information).

The high electrochemical reversibility and structural stability of $Na_{4/7}[Mn_{6/7}(\square_{Mn})_{1/7}]O_2$ between 1.5 and 4.4 V (Figure 1) can be well explained with the calculated energy barrier for the Mn-ion migration. Figure 5d shows that the energy barrier of Mn migration is over 4.0 eV for $Na_{4/7}[Mn_{6/7}(\square_{Mn})_{1/7}]O_2$. This actually demonstrates the impossibility for the Mn ions to migrate into the Na layer and the structural stability of $Na_{4/7}[Mn_{6/7}(\square_{Mn})_{1/7}]O_2$ upon Na-ion extraction. The energy barrier is still as high as 2.8 eV even when 2/7 Na is extracted ($Na_{2/7}[Mn_{6/7}(\square_{Mn})_{1/7}]O_2$), close to the state when ≈0.33 Na f.u.$^{-1}$ is extracted from $Na_{4/7}[Mn_{6/7}(\square_{Mn})_{1/7}]O_2$ (charged to 4.4 V; Figure 5e). These explain the STEM observations that no Mn ions are detected in the Na layer (Figure 3e,f) and the structure remains unchanged when the Na ions are extracted ($Na_{4/7}[Mn_{6/7}(\square_{Mn})_{1/7}]O_2 \rightarrow Na_{2/7}[Mn_{6/7}(\square_{Mn})_{1/7}]O_2$).

Figure S15 (Supporting Information) schematically displays the structural evolution of $Na_{4/7+x}[Mn_{6/7}(\square_{Mn})_{1/7}]O_2$ on the basis of the DFT calculations, verifying the stable layered structure (Figure S15a, Supporting Information) and the Mn−O bond lengths (Figure S15c, Supporting Information). Figure S15b (Supporting Information) further indicates that the vacancies in the $[Mn_{6/7}(\square_{Mn})_{1/7}]O_2$ slabs remain there during Na-ion extraction. Figure S16 (Supporting Information) summarizes the calculated Mn−O and Mn−Mn bond lengths at various Na extraction states, demonstrating the stability of the $[Mn_{6/7}(\square_{Mn})_{1/7}]O_2$ slabs.

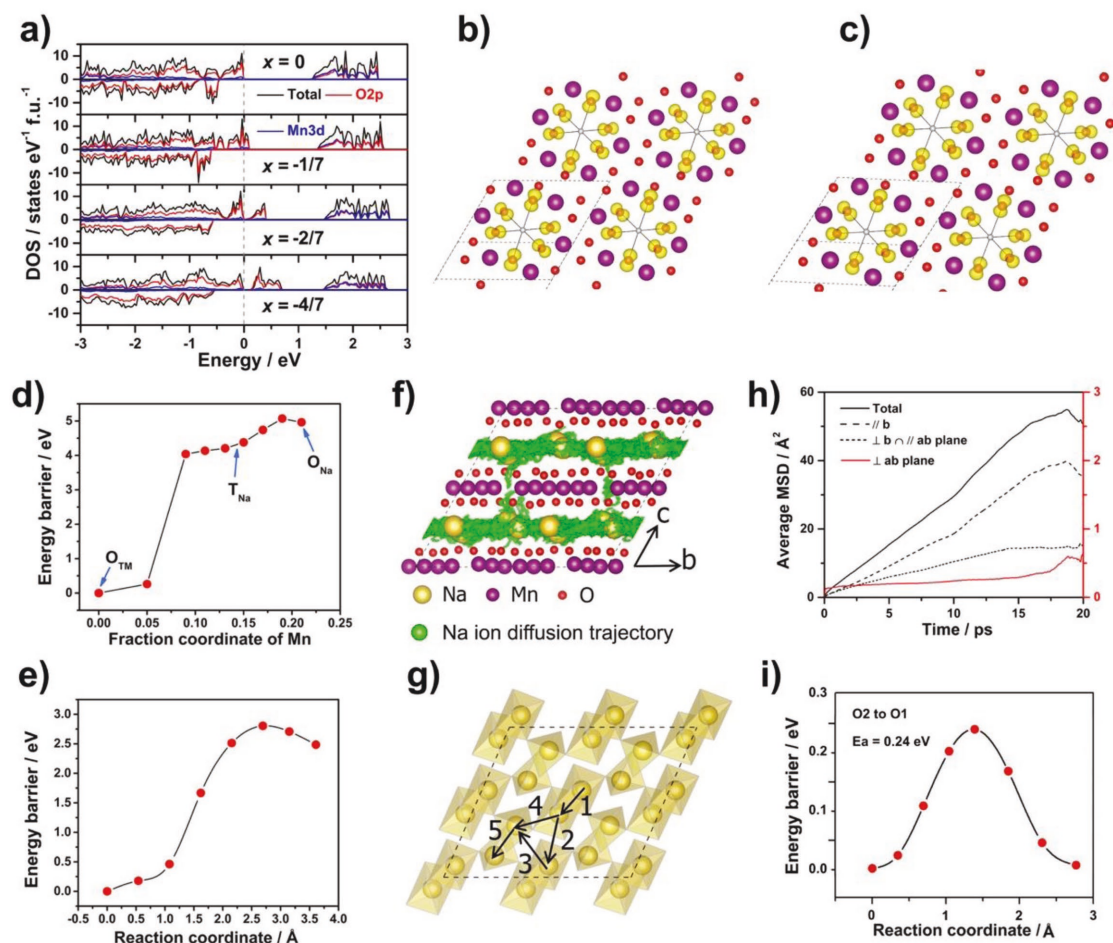Although we cannot directly correlate the presence of the vacancies in an oxide material with the migration energy

Figure 5. a) DOS of $Na_{4/7+x}[Mn_{6/7}]O_2$ at various charged states ($x \leq 0$). The Fermi level is set to zero. The charge distribution of electrons with energy b) from −0.45 to 0.0 eV and c) from −0.75 to 0.0 eV in $Na_{4/7}Mn_{6/7}O_2$. The number of electrons is about 1/7 for the former and 2/7 for the latter on the basis of DOS. The purple, red, and gray balls represent the Mn ions, O ions, and O vacancies, respectively. The yellow contour around the O ions represent the charge distribution. d) The dependence of the total energy on the z-coordinate of the Mn ion in $Na_{4/7}[Mn_{6/7}(\square_{Mn})_{1/7}]O_2$ and e) the energy barrier of Mn migration into Na layer in $Na_{2/7}[Mn_{6/7}(\square_{Mn})_{1/7}]O_2$. f) Calculated distribution of the probability density, g) the possible migration pathways of the Na ions, h) the mean square displacement (MSD) projected along different directions in $Na_{4/7}[Mn_{6/7}(\square_{Mn})_{1/7}]O_2$ at 2000 K, and i) the energy barriers of Na migration along the favorable pathway.

barrier of its transition metal ions, a simple comparison of the migration energy barrier between some popular vacancy-free cathode materials and the present vacancy-containing $Na_{4/7}[Mn_{6/7}(\square_{Mn})_{1/7}]O_2$ indicates that the migration energy barrier of the transition metals in the former is much lower than in the latter (Table S2, Supporting Information). Therefore, we believe that the presence of the vacancies makes the structure more stable and flexible upon extraction and insertion of large amounts of the alkali metal ions. In contrast, the structure of the $[Mn_{2/3}Li_{1/3}]O_2$ slab is rigid and Mn migration and O_2 release often occur in the vacancy-free Li_2MnO_3-based Li-rich oxide materials.

Finally, we perform first-principle molecular dynamics simulations to examine the transport of Na ions in $Na_{4/7}[Mn_{6/7}(\square_{Mn})_{1/7}]O_2$. The distribution probability density of the Na ions shows that they prefer to diffuse in the *ab*-plane as opposed to the normal direction (Figure 5f). The mean square displacement (MSD) in the three directions reveals that the MSD in the *b*-direction is much larger than that in the other

two (Figure 5h). The most favorable diffusion path is from an octahedral site to its neighboring octahedral site (Figure 5g,i), with an energy barrier of 0.24 eV, lower than that of any other paths (e.g., 0.74 eV from the tetrahedral site in the Na layer to the vacancy site ($\square_{Mn}$); Figure S17, Supporting Information).

Figure S18 (Supporting Information) shows the cycling performance of $Na_{4/7}[Mn_{6/7}(\square_{Mn})_{1/7}]O_2$. When it is cycled between 1.5 and 4.4 V, the reversible capacity decreases from 220 to 150 mAh g^{-1} in 20 cycles due to electrolyte decomposition at high voltages (≈4.4 V). The cycling stability becomes much better after the voltage window is tuned to 2.3–4.2 V; a capacity retention of 100% is obtained in 45 cycles (Figure 1e). As is demonstrated with the above characterizations, the charge compensation within this voltage range is accomplished by the redox reaction of the oxygen. Therefore, the improved cycling performance in this narrowed voltage window further shows, from the other side of the same coin, that the charge compensation by the reversible oxygen redox reaction and the flexible structure take an important role in utilizing

**ADVANCED
SCIENCE NEWS**

www.advancedsciencenews.com

**ADVANCED
ENERGY
MATERIALS**

www.advenergymat.de

$Na_{4/7}[Mn_{6/7}(\square_{Mn})_{1/7}]O_2$ as a promising cathode material for the NIBs.

3. Discussion

A simple comparison on the structural characteristics of the Li-rich manganese oxides (e.g., Li_2MnO_3) and the present $Na_{4/7}[Mn_{6/7}(\square_{Mn})_{1/7}]O_2$ helps to understand the high structural stability and the reversibility of the oxygen redox reaction in this material. Li_2MnO_3 is an important building block for the Li-rich oxide cathode material.[18] Similar to the present $Na_{4/7}[Mn_{6/7}(\square_{Mn})_{1/7}]O_2$, the Mn ions in Li_2MnO_3 cannot be oxidized till the end of the initial charge (usually cutoff at 4.8 V). Therefore, activation of Li_2MnO_3 is realized by the oxygen oxidation. However, the reversibility of the oxygen redox reaction in Li_2MnO_3 is very poor due to significant O_2 evolution and Mn-ion migration, and the resultant structural degradation. In contrast, such structural and performance decay is not observed in $Na_{4/7}[Mn_{6/7}(\square_{Mn})_{1/7}]O_2$.

The basic structural unit in Li_2MnO_3 is the symmetric MnO_6 octahedron, in which four of the Mn−O bonds have the same length while the other two Mn−O bonds have another length. There is no vacancy in the MnO_6 octahedron. Therefore, no Li ions can be inserted in it. Different from Li_2MnO_3, the lengths of all the six Mn−O bonds in the basic structural unit of $Na_{4/7}[Mn_{6/7}(\square_{Mn})_{1/7}]O_2$, the $[Mn_{6/7}(\square_{Mn})_{1/7}]O_2$ slab, are different from each other and there exist periodic vacancies in the Mn−O layer. The presence of the intrinsic vacancies makes this unit deformed and a total of 0.57 Na f.u.$^{-1}$ can be inserted (0.14 Na f.u.$^{-1}$ inserted in the Mn−O layer and 0.43 Na f.u.$^{-1}$ inserted in the Na layer) in $Na_{4/7}[Mn_{6/7}(\square_{Mn})_{1/7}]O_2$ without damaging its structural skeleton.

It is well known that the deformation of MO_6 (M = Mn and Mo) octahedrons during (de)sodiation enhances the migration of the transition metal M, which in turn drives undesirable structural changes, leading to performance decay in Li_2MO_3.[3,8] Thanks to the presence of the native vacancies in $Na_{4/7}[Mn_{6/7}(\square_{Mn})_{1/7}]O_2$, the MnO_6 octahedrons are structurally more robust and tolerant toward (de)sodiation because there is more room for the rearrangements of the Na ions and the neighboring MnO_6 octahedrons, yielding less additional distortions to the $[Mn_{6/7}(\square_{Mn})_{1/7}]O_2$ slab. In other words, the native vacancies in this material enhance the structural stability and the reversibility of the oxygen redox reactions. The structural analysis has shown that $Na_{4/7}[Mn_{6/7}(\square_{Mn})_{1/7}]O_2$ displays a zero-strain characteristic upon Na-ion extraction or insertion, up to 0.76 Na f.u.$^{-1}$ (Figure 1). In contrast, Li_2MnO_3 without native vacancies experiences a layered to spinel-like structural change upon Li removal.[2f] Therefore, we believe that the presence of the ordered native vacancies in $Na_{4/7}[Mn_{6/7}(\square_{Mn})_{1/7}]O_2$ can self-regulate its deformation, enhance the structure robustness, and improve the electrochemical reversibility.[23] In fact, there are many materials with native vacancies, such as $Li_{4/7}[Mn_{6/7}(\square_{Mn})_{1/7}]O_2$, which are expected to exhibit similar structural robustness and aging resistance in electrochemical applications. Thus, our work could have important impact on future selection, design, and preparation of high-performance cathode materials.

4. Conclusions

In summary, a novel air-stable layer-structured Mn-based oxide $Na_{4/7}[Mn_{6/7}(\square_{Mn})_{1/7}]O_2$ was synthesized by a simple solid-state reaction. Different from the traditional layered materials, this material contains large amount of intrinsic periodic vacancies in its $[Mn_{6/7}(\square_{Mn})_{1/7}]O_2$ slabs. With these native vacancies, it shows high structural flexibility and is zero-strain upon Na extraction and insertion in the slabs as well as in the interlayers between them. The above electrochemical evaluation, physical characterization, and DFT calculations indicate that the presence of the intrinsic vacancies is key to achieving the highly reversible O redox reaction in the material and its high structural stability. The intrinsic vacancies in the slabs, the vacancy-induced uneven lengths of the Mn−Mn and Mn−O bonds (or the asymmetric $[Mn_{6/7}(\square_{Mn})_{1/7}]O_2$ slab), and the charge compensation by Mn redox reaction ensure the immobility of the Mn and O ions and the structural robustness of the material at low to middle charge voltages (3/7 Na f.u.$^{-1}$ extracted/inserted below 2.3 V). Above 2.3 V, when the charge compensation by oxygen redox reaction become unavoidable, the presence of the vacancies in the Mn−O layer, the uneven lengths of the Mn−Mn and Mn−O bonds, and the less Na extraction (than in Li-rich Mn-based oxides) make it possible that the oxygen does not need to provide so much charge compensation as in the general Li-rich oxide cathode (0.33 Na f.u.$^{-1}$ for $Na_{4/7}[Mn_{6/7}(\square_{Mn})_{1/7}]O_2$ vs 2.0 Li f.u.$^{-1}$ in Li_2MnO_3). The above features assign $Na_{4/7}[Mn_{6/7}(\square_{Mn})_{1/7}]O_2$ with excellent electrochemical performances as a cathode material for the NIBs, delivering a high capacity of 220, 96 mAh g^{-1} of which is from the oxygen redox reaction between 2.3 and 4.2 V. Therefore the native $\square_{Mn}$ vacancies in the Mn−O layer take critical roles in enhancing the structural stability and the highly reversible oxygen redox reactions in the $Na_{4/7}[Mn_{6/7}(\square_{Mn})_{1/7}]O_2$. These findings provide new ideas on selecting and designing new cathode materials with high capacity and structural stability.

Supporting Information

Supporting Information is available from the Wiley Online Library or from the author.

Acknowledgements

Conflict of Interest

The authors declare no conflict of interest.

Keywords

cathode materials, charge compensation, oxygen redox, sodium manganese oxide, zero-strain

[1] J. B. Goodenough, K. S. Park, *J. Am. Chem. Soc.* **2013**, *135*, 1167.

[2] a) M. Sathiya, G. Rousse, K. Ramesha, C. P. Laisa, H. Vezin, M. T. Sougrati, M. L. Doublet, D. Foix, D. Gonbeau, W. Walker, A. S. Prakash, M. Ben Hassine, L. Dupont, J. M. Tarascon, *Nat. Mater.* **2013**, *12*, 827; b) P. E. Pearce, A. J. Perez, G. Rousse, M. Saubanere, D. Batuk, D. Foix, E. McCalla, A. M. Abakumov, G. Van Tendeloo, M.-L. Doublet, J.-M. Tarascon, *Nat. Mater.* **2017**, *16*, 580; c) Y. R. Gao, X. F. Wang, J. Ma, Z. X. Wang, L. Q. Chen, *Chem. Mater.* **2015**, *27*, 3456; d) A. K. Shukla, Q. M. Ramasse, C. Ophus, H. Duncan, F. Hage, G. Chen, *Nat. Commun.* **2015**, *6*, 8711; e) S. Kim, M. Aykol, V. I. Hegde, Z. Lu, S. Kirklin, J. R. Croy, M. M. Thackeray, C. Wolverton, *Energy Environ. Sci.* **2017**, *10*, 2201; f) B. Li, D. Xia, *Adv. Mater.* **2017**, *29*, 1701054.

[3] Y. Gao, J. Ma, Z. Wang, G. Lu, L. Chen, *Phys. Chem. Chem. Phys.* **2017**, *19*, 7025.

[4] a) R. Shunmugasundaram, R. Senthil Arumugam, J. R. Dahn, *Chem. Mater.* **2015**, *27*, 757; b) S. Muhammad, H. Kim, Y. Kim, D. Kim, J. H. Song, J. Yoon, J.-H. Park, S.-J. Ahn, S.-H. Kang, M. M. Thackeray, W.-S. Yoon, *Nano Energy* **2016**, *21*, 172; c) W. Liu, P. Oh, X. Liu, S. Myeong, W. Cho, J. Cho, *Adv. Energy Mater.* **2015**, *5*, 1500274; d) H. Liu, Y. Chen, S. Hy, K. An, S. Venkatachalam, D. Qian, M. Zhang, Y. S. Meng, *Adv. Energy Mater.* **2016**, *6*, 1502143;

[5] A. J. Perez, Q. Jacquet, D. Batuk, A. Iadecola, M. Saubanère, G. Rousse, D. Larcher, H. Vezin, M.-L. Doublet, J.-M. Tarascon, *Nat. Energy* **2017**, *2*, 954.

[6] C. Zhan, Z. Yao, J. Lu, L. Ma, V. A. Maroni, L. Li, E. Lee, E. E. Alp, T. Wu, J. Wen, Y. Ren, C. Johnson, M. M. Thackeray, M. K. Y. Chan, C. Wolverton, K. Amine, *Nat. Energy* **2017**, *2*, 963.

[7] S. Liu, Z. Liu, X. Shen, W. Li, Y. Gao, M. N. Banis, M. Li, K. Chen, L. Zhu, R. Yu, Z. Wang, X. Sun, G. Lu, Q. Kong, X. Bai, L. Chen, *Adv. Energy Mater.* **2018**, *8*, 1802105.

[8] Z. Zhu, A. Kushima, Z. Yin, L. Qi, K. Amine, J. Lu, J. Li, *Nat. Energy* **2016**, *1*, 16111.

[9] X. Lu, L. Gu, Y. S. Hu, H. C. Chiu, H. Li, G. P. Demopoulos, L. Chen, *J. Am. Chem. Soc.* **2015**, *137*, 1581.

[10] G.-N. Zhu, Y.-G. Wang, Y.-Y. Xia, *Energy Environ. Sci.* **2012**, *5*, 6652.

[11] a) Y. Wang, X. Yu, S. Xu, J. Bai, R. Xiao, Y. S. Hu, H. Li, X. Q. Yang, L. Chen, X. Huang, *Nat. Commun.* **2013**, *4*, 2365; b) J. Kim, G. Yoon, M. H. Lee, H. Kim, S. Lee, K. Kang, *Chem. Mater.* **2017**, *29*, 7826.

[12] H. L. Pan, Y. S. Hu, L. Q. Chen, *Energy Environ. Sci.* **2013**, *6*, 2338.

[13] X. H. Ma, H. L. Chen, G. Ceder, *J. Electrochem. Soc.* **2011**, *158*, A1307.

[14] A. Mendiboure, C. Delmas, P. Hagenmuller, *J. Solid State Chem.* **1985**, *57*, 323.

[15] Y. Wang, J. Liu, B. Lee, R. Qiao, Z. Yang, S. Xu, X. Yu, L. Gu, Y. S. Hu, W. Yang, K. Kang, H. Li, X. Q. Yang, L. Chen, X. Huang, *Nat. Commun.* **2015**, *6*, 6401.

[16] X.-P. Gao, H.-X. Yang, *Energy Environ. Sci.* **2010**, *3*, 174.

[17] R. Robert, C. Bünzli, E. J. Berg, P. Novák, *Chem. Mater.* **2015**, *27*, 526.

[18] N. Yabuuchi, K. Yoshii, S.-T. Myung, I. Nakai, S. Komaba, *J. Am. Chem. Soc.* **2011**, *133*, 4404.

[19] V. R. Galakhov, M. Demeter, S. Bartkowski, M. Neumann, N. A. Ovechkina, E. Z. Kurmaev, N. I. Lobachevskaya, Y. M. Mukovskii, J. Mitchell, D. L. Ederer, *Phys. Rev. B* **2002**, *65*, 113102.

[20] D. Bélanger, T. Brousse, J. W. Long, *J. Electrochem. Soc. Interface* **2008**, *155*, 49.

[21] C. Julien, M. Massot, R. Baddour-Hadjean, S. Franger, S. Bach, J. P. Pereira-Ramos, *Solid State Ionics* **2003**, *159*, 345.

[22] D.-H. Seo, J. Lee, A. Urban, R. Malik, S. Kang, G. Ceder, *Nat. Chem.* **2016**, *8*, 692.

[23] A. Manthiram, K. Chemelewski, E.-S. Lee, *Energy Environ. Sci.* **2014**, *7*, 1339.